

# Model for a Noise Matched Phased Array Feed

D. Anish Roshi, *Member, IEEE*, W. Shillue, *Member, IEEE*, and J. Richard Fisher, *Member, IEEE*

**Abstract**—We present a model for a Noise Matched Phased Array Feed (PAF) system and compare model predictions with the measurement results. The PAF system consists of an array feed, a receiver, a beamformer and a parabolic reflector. The novel aspect of our model is the characterization of the PAF system by a single matrix. This characteristic matrix is constructed from the open-circuit voltage covariance at the output of the PAF due to signal from the observing source, ground spillover noise, sky background noise and (low-noise) amplifier (LNA) noise. The best signal-to-noise ratio on the source achievable with the PAF system will be the maximum eigenvalue of the characteristic matrix. The voltage covariance due to signal and spillover noise are derived by applying the Lorentz reciprocity theorem. The receiver noise covariance and noise temperature are obtained in terms of Lange invariants such that they are suitable for noise matching the array feed. The model predictions are compared with the measured performance of a 1.4 GHz, 19-element, dual-polarized PAF on the Robert C. Byrd Green Bank Telescope.<sup>1</sup> We show that the model predictions, obtained with an additional noise contribution due to the measured losses ahead of the low-noise amplifier, compare well with the measured ratio of system temperature to aperture efficiency as a function of frequency and as a function of offset from the boresight. Further, our modeling indicates that the bandwidth over which this ratio is optimum can be improved by a factor of at least two by noise matching the PAF with the LNA.

**Index Terms**—Antenna Array Feeds, Antenna array mutual coupling, Amplifier noise, Phased Arrays

## I. INTRODUCTION

THE extreme faintness of celestial radio sources motivates the use of telescopes with large collecting areas. The field-of-view (FoV) of a single-dish telescope that uses a single feed to receive signals decreases in proportion to the collecting area. Traditionally, array feeds consisting of multiple horn antennas have been used to increase the FoV of such telescopes. The antennas in such arrays cannot be closely packed since the feeds are physically large as they have to illuminate the reflector efficiently. Consequently, the telescope beams corresponding to the different elements are separated by considerably more than the half-power beamwidth (HPBW). The non-overlapping beams reduce the mapping efficiency. Feeds consisting of dense, electrically small antenna arrays as a means to overcome this limitation are now of significant

interest [1]–[8]. These dense arrays sample the focal field pattern of the telescope. Multiple beams are then formed by combining the signals sampled by the array elements with complex weights that form an efficient reflector illumination. Such arrays are referred to as Phased Array Feeds (PAF). The beams formed using a PAF can fully sample the FoV. Additionally, a PAF can be used to improve spillover efficiency as well as the illumination of the dish. However, mutual coupling between array elements is a major hurdle in designing a low-noise PAF (see, for example, [9]). Mutual coupling modifies the element radiation patterns. It also couples amplifier noise between signal paths. Therefore, detailed electromagnetic, noise and network modeling are needed to design a PAF for radio astronomy applications [10].

Several research groups have analyzed and modeled the noise performance [11]–[16] and electromagnetic properties of a PAF on a reflector antenna [17], [18]. A working expression for the covariance matrix of the signal due to a source at the output of the PAF was provided by Warnick & Jeffs (2008) [19] and corresponding matrix for spillover noise was derived by Warnick & Jeffs (2006) [20] (see also [21]). These matrices were then used to provide expression for aperture and spillover efficiencies [19], [20]. The receiver noise covariance matrix for a PAF was derived by Warnick & Jensen (2005) [11] (see also [12]). Hay (2010) [18] (see also [14]) analyzed the noise performance of a PAF with a lossless input matching network in terms of Lange invariants. He also provided optimum solutions for the matching network for maximum signal-to-noise ratio (SNR) and total efficiencies (see [15] and references therein for other optimization). Finally, simplification of the PAF receiver noise model has been discussed by Ivashina et al. (2008) [22] to better understand the factors affecting system sensitivity.

In this paper, we apply the Lorentz reciprocity theorem to a PAF mounted at the prime focus of a reflector telescope to derive a new expression for the signal covariance matrix. We also provide a new expression for the receiver noise covariance matrix and noise temperature in terms of the Lange invariants, which are advantageous for numerically optimizing the system performance with a lossless matching network (see also [23]). A novel aspect of our modeling is the introduction of a single matrix, referred to as the characteristic matrix of the PAF system, constructed from these covariance matrices to express the SNR at the output of the PAF. The PAF system is described in Section II. A summary of the novel aspects of our PAF model and its implementation are presented in Section III. We then compare the model predictions with measurements made with a 1.4 GHz, 19-element dual-polarized PAF on the Green Bank Telescope (GBT) [24]. The results of the comparative study are given in Section IV. The main results of the paper are summarized in the Section V. A list of mathematical symbols

D. A. Roshi was with the National Radio Astronomy Observatory (NRAO), Charlottesville. He is currently with the Arecibo Observatory, Arecibo, PR 00612. W. Shillue and J. R. Fisher are with the NRAO, 520 Edgemont Road, Charlottesville, VA 22903 USA e-mail: aroshi@naic.edu, bshillue@nrao.edu, rfisher@nrao.edu.

The National Radio Astronomy Observatory is a facility of the National Science Foundation operated under a cooperative agreement by Associated Universities, Inc.

Manuscript received ; revised .

<sup>1</sup>The Green Bank Observatory is a facility of the National Science Foundation operated under a cooperative agreement by Associated Universities, Inc.

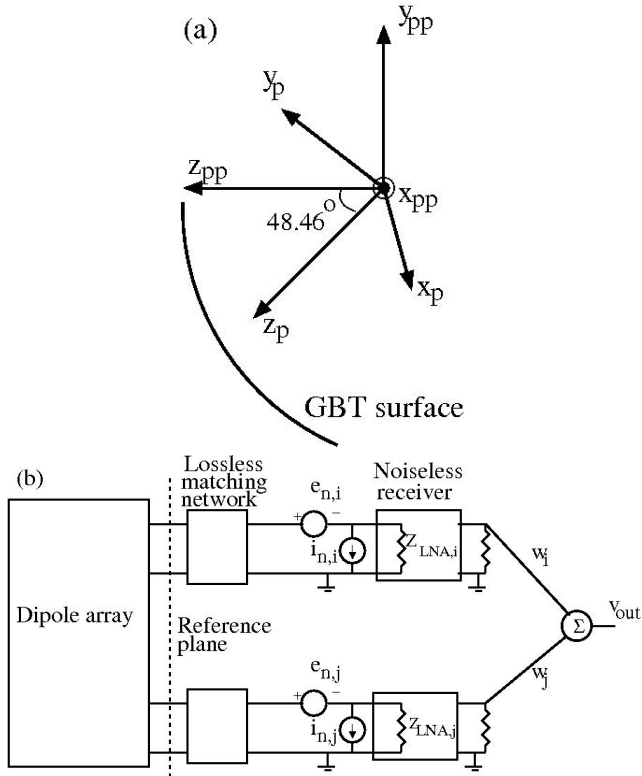


Fig. 1. The PAF system. (a) A schematic of the GBT reflector geometry. The equation of the reflector surface is expressed in the  $x_{pp} - y_{pp} - z_{pp}$  coordinate system. The  $x_p - y_p - z_p$  coordinate system is used to describe the properties of the PAF. The origins of the two coordinate systems coincide and are located at the prime focus of the reflector. The orientation of the  $x_p - y_p - z_p$  coordinate system relative to the  $x_{pp} - y_{pp} - z_{pp}$  is obtained through two rotations: a rotation about  $x_p$  by  $48.46^\circ$  as shown and a rotation about  $z_p$  by  $45^\circ$ . The ground plane of the PAF coincides with the  $x_p - y_p$  plane and the X and Y polarization dipoles are parallel to  $x_p$  and  $y_p$  axes respectively. (b) The PAF, noise matching network, receiver system and the beamformer. The noise voltage and current fluctuations are related to the noise parameters  $R_{n_i}$ ,  $g_{n_i}$  and  $\rho_i$  of the LNA:  $\langle e_{n,i}^2 \rangle = 4k_B T_0 R_{n_i}$ ,  $\langle i_{n,i}^2 \rangle = 4k_B T_0 g_{n_i}$ , and  $\rho_i = \frac{\langle e_{n,i}^* i_{n,i} \rangle}{\sqrt{\langle e_{n,i}^2 \rangle \langle i_{n,i}^2 \rangle}}$ , where  $k_B$  is the Boltzmann constant and  $T_0 = 290$  K.

used in the paper is given in Appendix B.

## II. THE PAF SYSTEM

The PAF system consists of a dual-polarized dipole array followed by noise matching networks, LNAs and receiver system, a beamformer and a parabolic reflector or telescope (see Fig. 1). In Fig. 1a, we show an off-axis reflector, representing the surface of the GBT. The projected surface of the reflector in the boresight direction (i.e perpendicular to the  $x_{pp} - y_{pp}$  plane in Fig. 1a) is circular with a diameter 100 m and the focal length over diameter ratio is 0.6. Further details of the GBT geometry are available in [25], [26]. The PAF is mounted at the prime focus with the plane of the array at an angle  $48.46^\circ$  from the  $x_{pp} - y_{pp}$  plane (see Fig. 1a).

The dipole array consists of 19 dual-polarized elements (see Fig 2). The dipole shape was optimized for active impedance match to the LNA and for maximum sensitivity on the GBT over a FoV of  $\sim 20$  arcminutes [15], [17]. The frequency range used for optimization was  $\geq 150$  MHz centered at 1350

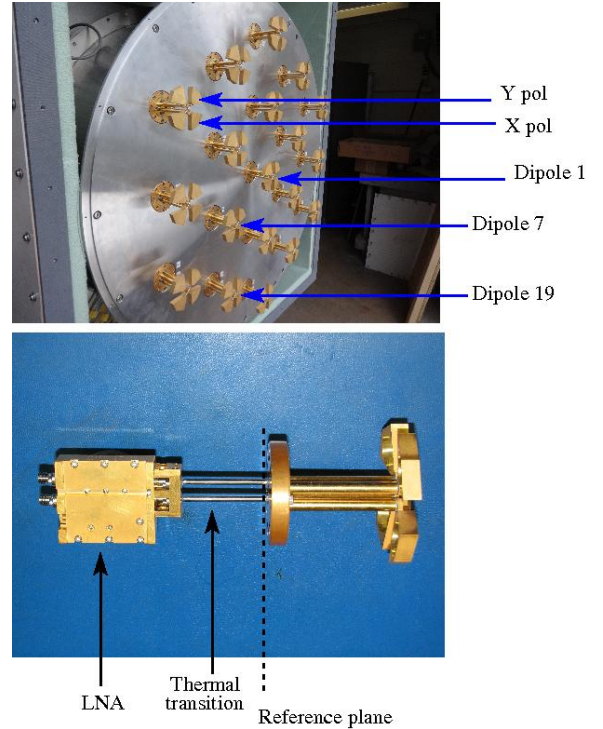


Fig. 2. The 19-element dual-polarized dipole array is shown on the top. The array is designed to operate near 1350 MHz with a bandwidth  $\geq 150$  MHz. The dipoles are numbered counter clockwise along each ‘ring’. The dipole designation for the X and Y polarizations are marked. A dual polarized dipole pair along with the thermal transitions and LNAs are shown in the bottom. The reference plane marked on the figure corresponds to that shown in Fig. 1. The length of the thermal transition (6.4 cm) is fixed for the actual array, but we have varied its length in the PAF modeling program to noise match the array to the LNA.

MHz. A balun converts the signals received by the dipoles to unbalanced signals, which are available at the output of a transmission line with characteristic impedance  $z_0$ , which is same as the  $50 \Omega$  reference impedance. The transmission line terminates at the ‘reference plane’ marked on Fig 1b (see also Fig. 2). The dipole array, balun, ground plane and the transmission line together is referred to as the PAF. Further details of the PAF is available in [24].

The PAF is followed by a two-port, lossless matching network, which in the simplest case can be a transmission line of length  $L_{trans}$ . The transmission line in the measurement system is the thermal transition (see Fig. 2) with  $L_{trans} \sim 6.4$  cm and characteristic impedance of  $50 \Omega$ . The thermal transition is made of air-core stainless steel co-axial transmission line with the central stainless steel conductor coated with copper and gold of  $5 \mu\text{m}$  thickness. As discussed in Section IV, we have used this transmission line as the matching network in the PAF model and have varied  $L_{trans}$  for all dipoles between 3 and 20 cm for noise matching the PAF to the LNA. The LNAs are located at the end of the matching network. The LNAs used for the measurements were cryogenic Silicon Germanium Heterojunction Bipolar Transistor (SiGe HBT) amplifiers cooled to about 15 K [24], [27]. The  $i^{th}$  LNA has an input impedance of  $Z_{LNA_i} \sim 50 \Omega$  and gain  $\sim 38$  dB. The input impedance of the receiver system is

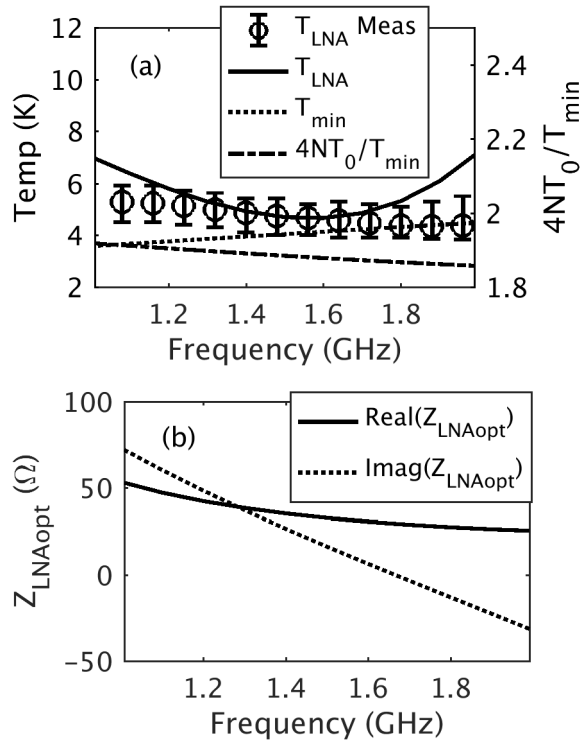


Fig. 3. (a) The measured mean noise temperature vs frequency of the LNA and its peak-to-peak scatter are marked in circles with ‘error bar’. The mean (4.85 K) and scatter (1.4 K) are obtained from the measurements of 38 LNAs. The noise temperature prediction from the noise model of the LNA is shown with continuous line. The noise parameter  $T_{min}$  and  $4NT_0/T_{min}$  are plotted in dotted and dashed lines respectively. (b) The real (continuous line) and imaginary parts (dotted line) of the  $Z_{LNAopt}$  are plotted as a function of frequency.

transformed by the matching network to  $Z_{in_i}$  at the reference plane. The noise properties of the LNA are usually specified by the noise parameters  $R_{n_i}$ , the noise resistance,  $g_{n_i}$ , the noise conductance, and  $\rho_i$ , the complex noise correlation [28] (see also Fig. 1b). An equivalent set of noise parameters used in radio astronomy are  $Z_{LNAopt_i}$ , the optimum impedance and the Lange invariants,  $T_{min_i}$  (the minimum noise temperature) and  $N_i$  [28], [29]. The relationship between the two sets of noise parameters is discussed in [28]. The latter set of noise parameters is advantageous when lossless networks are used for noise matching. This is because the noise parameters  $T_{min_i}$  and  $N_i$  remain invariant when they are transformed through a lossless network placed at the input of the LNA and  $Z_{LNAopt_i}$  transforms to  $Z_{opt_i}$  like a normal impedance transformation. Fig. 3 shows the noise parameters vs frequency obtained from the noise model of the LNA. The predicted temperature from the noise model of the LNA is consistent with measurements in the frequency range 1.2 to 1.7 GHz (see Fig. 3) [27]. However, the model noise temperature deviates from measurement outside this frequency range. We are in the process of improving the noise model of the LNA and the results will be presented elsewhere.

In the measurement system, the signals from the output of the LNAs are further amplified, down-converted to basebands, digitized using analog-to-digital converters (ADC) and then followed by Fast Fourier Transform (FFT) engines to create

time series of complex voltage spectra (see [24] for a full description of the system). The basic signal processing done in a PAF system, referred to as *beamforming*, can be expressed as [30]

$$v_{out} = \sum_{i=1,M} w_i v_i = \mathbf{w}^T \tilde{\mathbf{V}} \quad (1)$$

where the elements of the voltage vector  $\tilde{\mathbf{V}}$  are the input complex voltages  $v_i$  from a spectral channel to the beamformer, the elements of the weight vector  $\mathbf{w}^T$  are the complex beamforming weights  $w_i$  and  $M = 19 \times 2$  is equal to the number of elements in the PAF. Multiple beams are formed by applying different sets of beamforming weights.

For modeling the PAF, its network property is specified by the (spectral) impedance matrix  $\mathbf{Z}$  and its electromagnetic property is specified by the *embedded beam patterns* [31] (see also [32], [33]). In this paper, we define the  $i^{th}$  embedded beam pattern,  $\psi_i^e(\vec{r})$ , as the radiation pattern of the PAF when  $i^{th}$  port is excited with 1 A and all other ports are open circuited. The position vector  $\vec{r}$  is defined in the  $x_p - y_p - z_p$  coordinate system (see Fig. 1a). There will be  $M = 19 \times 2$  embedded beam patterns for the dual polarized array. The beam pattern at the far-field can be expressed as an out-going spherical wave; i.e.  $\psi_i^e(\vec{r}) = \tilde{\Psi}_i^e(\theta, \phi) \frac{e^{j\vec{k} \cdot \vec{r}}}{r}$ , where  $\vec{k}$  is the propagation vector and  $r = |\vec{r}|$ . The radiation pattern of the PAF when excited by a set of arbitrary port currents  $\mathcal{J}_0_i$  is

$$\vec{\mathcal{E}}(\vec{r}) = \sum_{i=1,M} \mathcal{J}_0_i \psi_i^e(\vec{r}) = \mathbf{I}_0^T \tilde{\Psi}^e, \quad (2)$$

where  $\mathbf{I}_0$  is the vector of port currents and  $\tilde{\Psi}^e$  is the vector of embedded beam patterns. The  $\theta, \phi$  dependence of the far-field beam pattern can be written in a similar fashion:  $\vec{E}(\theta, \phi) = \mathbf{I}_0^T \tilde{\Psi}^e$ , where  $\tilde{\Psi}^e$  is a vector with elements  $\tilde{\Psi}_i^e$ . The unit of  $\vec{\mathcal{E}}$  is V/m, that of  $\psi_i^e$  is V/A/m, that of  $\vec{E}$  is V and that of  $\tilde{\Psi}_i^e$  is V/A.

The voltages, currents and field amplitudes are considered harmonic quantities and their values are specified as *peak* values ( $e^{j\omega t}$  term is omitted for simplicity) for the derivation of the open circuit voltage (Eq. 6) by applying Lorentz reciprocity theorem. When applying this result to the PAF system, we need to consider radiation field from the astronomical and thermal sources. These fields and the induced voltages at the output of the PAF as well as the noise due to the LNA are stochastic quantities. We treat these signals in the quasi monochromatic approximation and their amplitudes are taken as RMS (root mean square) values. In this treatment, for example, the flux density of a stochastic radiation field  $\vec{E}_{inc}$  is  $S = \frac{1}{Z_0} \langle \vec{E}_{inc} \cdot \vec{E}_{inc}^* \rangle$  and will have units  $W/m^2/Hz$ . The open circuit voltage covariance  $\langle \mathbf{V}_{oc} \mathbf{V}_{oc}^H \rangle$ , where  $\mathbf{V}_{oc}$  is the induced voltage due to stochastic field or noise, is average power dissipated by the noise in unit conductance and unit bandwidth or  $W/Hz/\Omega$ .

### III. PAF MODEL

One of the novel aspects of our PAF model is the introduction of a new matrix, referred to as the characteristic matrix, to concisely represent the PAF system. Further, we apply the

Lorentz reciprocity theorem [34] to derive a new expression for the signal covariance matrix. The receiver covariance matrix is obtained in terms of the Lange invariants so that it is suitable for noise matching the array feed to the LNA. We summarize below these new aspects of the PAF theory and also briefly describe its implementation.

### A. PAF Theory Revisited

The question posed to develop our model for a lossless PAF is: what is the maximum signal-to-noise ratio that can be obtained with a PAF system when observing a compact source (point source) at some angle  $\theta_s, \phi_s$  from the boresight direction? The answer to this question is given by the following theorem:

*Theorem:* Given (a) the (spectral) impedance matrix,  $\mathbf{Z}$ , and the embedded beam patterns,  $\vec{\psi}^e$ , of the PAF, (b) the LNA noise parameters,  $T_{min_i}, N_i$  and the transformed impedance,  $Z_{opt_i}$  and  $Z_{in_i}$ , (c) the telescope geometry and ground temperature, (d) the flux density and direction  $\theta_s, \phi_s$  of the observing source and (e) the off-source sky temperature, one can construct a characteristics matrix  $\mathbf{M}$  for the PAF system. Then the best signal-to-noise ratio on the source is the maximum eigenvalue,  $e_{max}$ , of  $\mathbf{M}$ .

1) *Characteristic Matrix and Proof of the Theorem:* The SNR when observing a source with the PAF system is defined as the ratio of increase in power spectral density at the output of a beam due to the source relative to the off-source spectral density (see Eq. 6 [19], [30]). This SNR at the beamformer output can be expressed in terms of the covariance of the open circuit voltages at the reference plane shown in Fig. 1 as

$$\text{SNR} = \frac{\mathbf{w}_1^H \mathbf{R}_{signal} \mathbf{w}_1}{\mathbf{w}_1^H \mathbf{N} \mathbf{w}_1} = \frac{\mathbf{w}_2^H \mathbf{M} \mathbf{w}_2}{\mathbf{w}_2^H \mathbf{w}_2} \quad (3)$$

where  $\mathbf{R}_{signal}$  is the open circuit covariance matrix due to signal from the source,

$$\mathbf{N} = \mathcal{N}\mathcal{N} \equiv \mathbf{R}_{spill} + \mathbf{R}_{rec} + \mathbf{R}_{sky} \quad (4)$$

is the sum of the open circuit noise covariance matrices due to spillover,  $\mathbf{R}_{spill}$ , receiver  $\mathbf{R}_{rec}$ , and sky background radiation,  $\mathbf{R}_{sky}$ ,

$$\mathbf{M} \equiv \mathcal{N}^{-1} \mathbf{R}_{signal} \mathcal{N}^{-1}, \quad (5)$$

is defined as the characteristics matrix. The relationship between the weight vectors are  $\mathbf{w}_1 = (\mathbf{Z}_{in}(\mathbf{Z} + \mathbf{Z}_{in})^{-1})^H \mathbf{G}^H \mathbf{w}$  and  $\mathbf{w}_2 = \mathcal{N} \mathbf{w}_1$ ,  $\mathbf{Z}_{in}$  is a diagonal matrix of elements  $Z_{in_i}$  and  $\mathbf{G}$  is a diagonal matrix with elements as the overall system gain. It follows from Eq. 3 that the maximum SNR is given by the maximum eigenvalue,  $e_{max}$ , of  $\mathbf{M}$ . The weight vector that needs to be applied in the beamformer can be obtained from the eigenvector corresponding to  $e_{max}$ .

2) *Open circuit voltage covariance:* Application of the Lorentz reciprocity theorem provides an expression for the open circuit voltage  $\mathbf{V}_{oc}$  at the output of the PAF as [32], [33]

$$\mathbf{V}_{oc} = \int_{A_{free}} \left( \vec{\psi}^{eT} \times \mathcal{I} \vec{\mathcal{H}}_r - \mathcal{I} \vec{\mathcal{E}}_r \times \vec{\mathcal{J}}^e \right) \cdot \hat{n} \, dA. \quad (6)$$

Here  $\vec{\mathcal{J}}^e$  is the vector of magnetic field patterns corresponding to the embedded beam pattern  $\vec{\psi}^e$ ,  $\vec{\mathcal{E}}_r$  and  $\vec{\mathcal{H}}_r$  are the incident

electric and magnetic fields respectively,  $\mathcal{I}$  is the identity matrix and  $\hat{n}$  is the unit normal inward to the elementary area  $dA$ . The surface of integration  $A_{free}$  is part of a closed surface outside the PAF.

3)  $\mathbf{R}_{signal}$ : We consider a compact astronomical source in the direction  $\theta_s, \phi_s$  from the boresight. For simplicity we assume that the source is unpolarized, which implies the following relationship between the flux density,  $S_{source}$ , and electric field of the incident plane wave,  $\vec{E}_{inc}$ , due to the source:  $\frac{S_{source}}{2} = \frac{1}{Z_0} \langle E_{inc,x} E_{inc,x}^* \rangle = \frac{1}{Z_0} \langle E_{inc,y} E_{inc,y}^* \rangle$ , where  $E_{inc,x}$  and  $E_{inc,y}$  are the two linearly polarized components of  $\vec{E}_{inc}$  and  $Z_0$  is the free space impedance. An appropriate closed surface, with the projected aperture plane (i.e. the telescope aperture plane projected onto a plane perpendicular to the direction of the source) as part of this surface can be considered for the evaluation of the integral in Eq. 6. The embedded beam patterns are propagated to the projected aperture plane for the evaluation of the integral (see Section III-B). The major contribution to the integral over  $A_{free}$  comes from the projected aperture plane [32]. The open circuit voltage covariance due the source can be obtained as

$$\mathbf{R}_{signal} = \frac{2S_{source}}{Z_0} \mathbf{C}_{I\psi} \quad (7)$$

where

$$\mathbf{C}_{I\psi} \equiv \left( \int_{A_{pap}} \vec{\psi}_{pap}^e \, dA \right) \cdot \left( \int_{A_{pap}} \vec{\psi}_{pap}^e \, dA \right)^H. \quad (8)$$

Here  $\vec{\psi}_{pap}^e$  is the vector of the propagated embedded beam pattern on the projected aperture plane  $A_{pap}$ . Note that  $\mathbf{C}_{I\psi}$  is a function of source position  $\theta_s, \phi_s$ . The unit of  $\mathbf{R}_{signal}$  is power spectral density per unit conductance.

We also provide an expression for the antenna temperature,  $T_A$ , which is a generalization of the equation for  $T_A$  for a reflector antenna with a single feed. The power spectral density due to the source, which is proportional to  $\mathbf{w}_1^H \mathbf{R}_{signal} \mathbf{w}_1$ , can be expressed as a physical temperature by comparing it with the power spectral density when the PAF system is at thermal equilibrium with the reference temperature  $T_0$  [35] (see also [21]):

$$\begin{aligned} T_A &= \frac{S_{source} A_{ap}}{2k_B} \left( \frac{\mathbf{w}_1^H \mathbf{C}_{I\psi} \mathbf{w}_1}{A_{ap} \mathbf{w}_1^H \mathbf{C}_{C\psi} \mathbf{w}_1} \right), \\ &= \frac{S_{source} A_{ap} \eta_{ap}}{2k_B}, \end{aligned} \quad (9)$$

where

$$\mathbf{C}_{C\psi} \equiv \int_{4\pi} \vec{\Psi}^e \cdot \vec{\Psi}^{eH} \, d\Omega, \quad (10)$$

and the aperture efficiency,  $\eta_{ap}$ , is defined in terms of the overlap integrals of the embedded beam patterns and the physical area of the telescope aperture,  $A_{ap}$ , as (see also [19])

$$\eta_{ap} \equiv \frac{\mathbf{w}_1^H \mathbf{C}_{I\psi} \mathbf{w}_1}{A_{ap} \mathbf{w}_1^H \mathbf{C}_{C\psi} \mathbf{w}_1}. \quad (11)$$

4)  $\mathbf{R}_{spill}$ : An expression for the covariance matrix of the voltage due to ground spillover radiation seen by the PAF is obtained in [19, their Eq. 9]. Applying Eq. 6 and following the arguments in [19]  $\mathbf{R}_{spill}$  can be readily expressed in terms of ground temperature,  $T_g$  ( $= 300$  K), and the overlap integral of the embedded beam patterns as [32], [33]

$$\mathbf{R}_{spill} = \frac{4k_B T_g}{Z_0} \mathbf{C}_{c\psi 1}, \quad (12)$$

where

$$\mathbf{C}_{c\psi 1} \equiv \int_{\Omega_{spill}} \tilde{\Psi}^e \cdot \tilde{\Psi}^{eH} d\Omega, \quad (13)$$

$\Omega_{spill}$  is the solid angle over which the PAF embedded beam patterns are receiving radiation from ground. Eq. 12 differs by a factor of 2 compared to Eq. 9 in [19] because  $\mathbf{R}_{spill}$  is the power spectral density per unit conductance (see Section II) and [19] provides the peak voltage covariance.

The spillover temperature,  $T_{spill}$ , as in the case of antenna temperature discussed above, is a generalization of the equation for  $T_{spill}$  for a reflector antenna with a single feed [32], [33]:

$$T_{spill} = T_g(1 - \eta_{spill}) \quad (14)$$

where

$$\eta_{spill} \equiv 1 - \frac{\mathbf{w}_1^H \mathbf{C}_{c\psi 1} \mathbf{w}_1}{\mathbf{w}_1^H \mathbf{C}_{c\psi} \mathbf{w}_1}. \quad (15)$$

In [19], Twiss's result [36] has been re-written in terms of the peak voltage covariance and so Eq. 15 and Eq. 16 in [19] give the same result.

5)  $\mathbf{R}_{rec}$ : The open circuit voltage covariance due to the LNA noise *in the absence of a matching network* is given by [15]

$$\begin{aligned} \mathbf{R}_{rec} &= \langle \mathbf{V}_{oc,r} \mathbf{V}_{oc,r}^H \rangle \\ &= \langle \mathbf{E}_n \mathbf{E}_n^H \rangle + \mathbf{Z} \langle \mathbf{I}_n \mathbf{E}_n^H \rangle + \\ &\quad \langle \mathbf{E}_n \mathbf{I}_n^H \rangle \mathbf{Z}^H + \mathbf{Z} \langle \mathbf{I}_n \mathbf{I}_n^H \rangle \mathbf{Z}^H. \end{aligned} \quad (16)$$

Here  $\langle \mathbf{E}_n \mathbf{E}_n^H \rangle$ ,  $\langle \mathbf{I}_n \mathbf{I}_n^H \rangle$  and  $\langle \mathbf{I}_n \mathbf{E}_n^H \rangle$  are diagonal matrices of noise fluctuations  $\langle e_{n,i}^2 \rangle$ ,  $\langle i_{n,i}^2 \rangle$  and their correlations  $\rho_i$  (see Fig. 1b). For identical LNAs connected to the PAF, i.e.  $R_{n_i} = R_n$ ,  $g_{n_i} = g_n$ ,  $\rho_i = \rho$ ,  $T_{min_i} = T_{min}$ ,  $N_i = N$  and  $Z_{LNAopt_i} = Z_{LNAopt}$  for all  $i$ , we get

$$\mathbf{R}_{rec} = 4k_B T_0 \left( R_n \mathbf{I} + \sqrt{R_n g_n} (\rho \mathbf{Z} + \rho^* \mathbf{Z}^H) + g_n \mathbf{Z} \mathbf{Z}^H \right). \quad (17)$$

We re-write  $\mathbf{R}_{rec}$  in terms of the Lange invariants, and the optimum impedance (see Appendix A),

$$\begin{aligned} \mathbf{R}_{rec} &= 4k_B T_{min} \frac{(\mathbf{Z} + \mathbf{Z}^H)}{2} \\ &+ 4k_B T_0 N \frac{(\mathbf{Z} - Z_{LNAopt} \mathbf{I})(\mathbf{Z} - Z_{LNAopt} \mathbf{I})^H}{\text{Re}\{Z_{LNAopt}\}}. \end{aligned} \quad (18)$$

The unit of  $\mathbf{R}_{rec}$  is power spectral density per unit conductance. When a matching network is introduced,  $\mathbf{R}_{rec}$  at the reference plane can be obtained by replacing  $Z_{LNAopt}$  with the transformed impedance  $Z_{opt}$  in Eq. 18.

The receiver temperature,  $T_{rec}$ , at the reference plane can be obtained from the power spectral density, which is proportional to  $\mathbf{w}_1^H \mathbf{R}_{rec} \mathbf{w}_1$ , as (see also [21])

$$T_{rec} = T_{min} + NT_0 \frac{\mathbf{w}_1^H (\mathbf{Z} - Z_{opt} \mathbf{I})(\mathbf{Z} - Z_{opt} \mathbf{I})^H \mathbf{w}_1}{\text{Re}\{Z_{opt}\} \frac{1}{2} \mathbf{w}_1^H (\mathbf{Z} + \mathbf{Z}^H) \mathbf{w}_1}. \quad (19)$$

Eq. 19 is a generalization of the expression for  $T_{rec}$  versus source impedance for a single antenna connected to a receiver (see Eq. 11 in [28]).

6)  $\mathbf{R}_{sky}$  and Losses in the PAF system: The sky background radiation has components due to cosmic microwave background (CMB), galactic and extragalactic radiation. We also include atmospheric radiation along with the sky contribution. When comparing the model results with measurement, it is also required to account for the losses in the PAF system ahead of the LNA. These losses are not included in the PAF theory and characterizing them is an ongoing research. In our model, the open circuit voltage covariance matrices due to these components are taken as [36]

$$\mathbf{R} \approx 2k_B T (\mathbf{Z} + \mathbf{Z}^H). \quad (20)$$

For  $\mathbf{R} = \mathbf{R}_{sky}$ , the covariance matrix due to sky radiation,  $T = T_{cmb} + T_{atmo} + T_{bg,\nu_0} \left(\frac{\nu}{\nu_0}\right)^{-2.7}$ , where  $T_{cmb} = 2.7$  K is the cosmic microwave background temperature,  $T_{atmo} = 2$  K [37] is the atmospheric radiation temperature (assumed to be frequency independent near 1.4 GHz) and  $T_{bg,\nu_0} = 0.7$  K is the galactic background radiation temperature at  $\nu_0 = 1.42$  GHz [38] and  $\nu$  is the frequency at which  $\mathbf{R}_{sky}$  is computed. For  $\mathbf{R} = \mathbf{R}_{loss}$ , the covariance matrix due to losses,  $T = T_{loss}$ , which is the physical temperature corresponding to the noise due to losses in the PAF system ahead of the LNA (see Section III-C). When comparing the model results with the measurements we have added  $\mathbf{R}_{loss}$  to  $\mathbf{N}$  in Eq. 4.

### B. The embedded beam pattern and the Impedance matrix

For the implementation of the theory presented above, the electromagnetic and network properties of the PAF were obtained using CST microwave studio (CST MWS<sup>2</sup>). A 3D model of a dual polarized element and balun were created in CST MWS by importing the Autodesk Inventor<sup>3</sup> CAD model of the dipole assembly and the array was created by placing copies of them. A rectangular ground plane of dimension 114.3 cm  $\times$  95.3 cm was added at a distance of 5.8 cm below the dipole elements. The full-wave 3D electromagnetic solver (transient solver in CST MWS) was used to get radiation patterns and scattering matrices of the PAF with hexahedral mesh size of  $\lambda/20$ . The solver would excite ports one at a time while all the other ports were terminated with the port impedance of 50  $\Omega$  to obtain the radiation pattern and scattering parameter. The final outputs of the CST simulation were these radiation patterns and scattering matrices for the different frequencies. The coordinate system that was used to obtain the radiation patterns corresponded to the  $x_p - y_p - z_p$  system defined in Section II (see Fig. 1a). A

<sup>2</sup><https://www.cst.com/products/estmws>

<sup>3</sup>[https://en.wikipedia.org/wiki/Autodesk\\_Inventor](https://en.wikipedia.org/wiki/Autodesk_Inventor)

MATLAB program was developed to compute the embedded beam patterns, as defined in Section II, from the CST outputs. The impedance matrix from the scattering parameter was also obtained using this program.

The embedded beam patterns need to be propagated to the projected aperture plane to compute  $\mathbf{R}_{signal}$  (see Eq. 7). We used geometric optics approximation to obtain the fields in the aperture plane [39]. The reflected field due to each incident embedded beam pattern on the telescope surface is first computed after accounting for the spherical spreading loss and then propagated to the aperture plane. Note that the geometric phases due to the location of feed elements (or in other words the excitation current distribution) relative to the coordinate origin were included in the computed embedded beam patterns (see [32] for further details).

### C. The losses ahead of the LNA

The receiver temperature of the PAF was measured in the outdoor test facility at the Green Bank Observatory (GBO) [24]. The hot/cold load method was used to measure the receiver temperature [21], [40], [41]. A warm absorber, placed close to the dipole array, formed the hot load. The array was pointed vertically to observe a cold sky region, which formed the cold load. The effect of ground scattered radiation was mitigated to some extent by placing a metallic cone around the array during measurement. These measurements provide the receiver noise covariance matrices for different frequencies which are then converted to temperature covariance matrices using the hot and cold load measurements [24]. The off-diagonal terms in the receiver temperature matrix have contributions from the mutual coupling in the array and the residual ground scattered radiation. These correlations can be canceled out to a large extent by taking the minimum eigenvalue of the temperature covariance matrix. This minimum eigenvalue we refer to as the minimum receiver temperature,  $T_{rec,min}$ . The measured  $T_{rec,min}$  as a function of frequency is shown in Fig. 8. The minimum difference of  $\sim 2.5$  K between  $T_{rec,min}$  and the measured amplifier noise temperature provides an upper limit to the losses ahead of the LNA [24]. The contributions to the uncertainty in the measured upper limit include (a) thermal uncertainty of the measurement ( $\sim 0.3$  K), (b) uncertainty in the LNA noise measurement ( $\sim 0.3$  K) and (c) uncertainty in the measured receiver temperature due to error in the hot and cold load temperatures ( $\sim 1$  K). Thus the net  $1\sigma$  uncertainty of this upper limit is  $\sim 1.1$  K.

### D. A computational model

A MATLAB<sup>4</sup> program was developed to apply the theory presented in Section III-A to the PAF system described in Section II. The program starts with the computation of  $\mathbf{R}_{rec}$ ,  $\mathbf{R}_{sky}$ ,  $\mathbf{R}_{spill}$  and  $\mathbf{R}_{signal}$ . These matrices are computed for a set of frequencies where impedance matrices and embedded beam patterns are available.  $\mathbf{R}_{signal}$  is computed for a set of directions to the source within the desired FoV. The characteristic matrix  $\mathbf{M}$  is then computed after adding  $\mathbf{R}_{loss}$

to the noise matrix. The maximum SNR and the corresponding weight vectors are obtained from  $\mathbf{M}$  for the set of frequencies and positions. The measured performance of the PAF system is usually expressed in  $T_{sys}/\eta$ , where  $T_{sys}$  is the system temperature and  $\eta$  is approximately the aperture efficiency  $\eta_{ap}$  of the telescope (assuming that the radiation efficiency of the PAF is close to unity). The model maximum SNR is converted to  $T_{sys}/\eta$  using the flux density of the source and the physical area of the telescope aperture [24]. The flux density models (typical uncertainty in flux density  $< 5\%$ ) of the observed sources are taken from Perley and Butler (2017) [42].

The model also provides the full polarization field patterns in the aperture plane and the far-field pattern of the telescope. These are provided for a specified set of weights. Further, the model computes the antenna temperature, aperture efficiency, spillover temperature and spillover efficiency for the specified weights.

## IV. COMPARISON WITH MEASUREMENT

The performance of a cryogenic 19-element dual-polarized PAF was measured on the GBT in March 2017 [24]. The observations that were made can be categorized into two groups. (1) Measurement of the performance of the boresight beam as a function of frequency. For this measurement, on-source and off-source voltage covariance on a set of calibrators were obtained. The covariances were measured for a set of frequencies in the range 1200 to 1500 MHz, each averaged over a bandwidth of  $\sim 300$  KHz. (2) Measurement of the system performance over the FoV. Voltage covariances on a grid of positions centered on a strong calibrator source Virgo A were obtained for these measurements at 1336 MHz.

The SNR on a source was obtained from the on-source and off-source measurements for both classes of observations. The beamformer weights were obtained by maximizing the SNR. The maximum SNR is expressed as the ratio of system temperature over efficiency,  $T_{sys}/\eta$ . The current measurements, however, do not provide separate values for  $T_{sys}$  and aperture efficiency.

The Y-polarization data set were affected by two faulty signal paths and telescope pointing offset. For comparison here, only a subset of Y-polarization data that are not severely affected by these problems are used (see [24] for further details).

### A. Boresight $\frac{T_{sys}}{\eta}$

The PAF model  $T_{sys}/\eta$  vs frequency for the boresight direction are obtained for different lengths,  $L_{trans}$ , for the thermal transition, which is used as the noise matching network in the model. These results are obtained with an additional contribution to noise matrix corresponding to  $T_{loss} = 0, 1,$  and  $2$  K to account for the losses ahead of the LNA (see Section III-C). The model results for  $L_{trans} = 9.1$  cm and for the three values of  $T_{loss}$  are shown in Fig. 4. The measured X polarizations  $T_{sys}/\eta$  vs frequency for the boresight taken from Roshi et al. (2018) [24, their Fig. 14] are included in Fig. 4 for comparison. As seen from Fig. 4, a reasonable fit to the data points is obtained with  $T_{loss} = 1$  K and  $L_{trans} = 9.1$

<sup>4</sup><https://www.mathworks.com/>

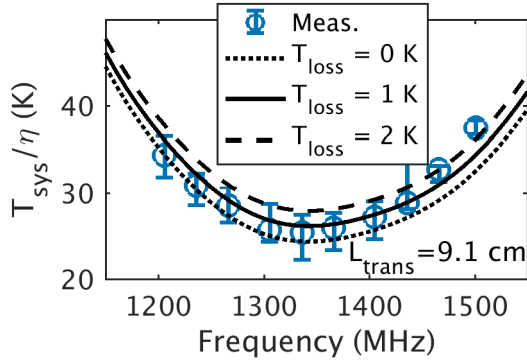


Fig. 4. The modeled boresight  $T_{sys}/\eta$  vs frequency for the X polarization compared with the measured values taken from Roshi et al. (2018) [24]. The median of measured values with peak-to-peak variation are shown in circles with ‘error bar’. The PAF model results for thermal transition length (used as matching network in the model)  $L_{trans} = 9.1$  cm are plotted for  $T_{loss} = 0, 1$  and 2 K.

cm. The physical length of the thermal transition in the PAF is about 6.4 cm. We attribute the discrepancy between the two physical lengths to unaccounted electrical length in the signal path.

The model predictions for different  $L_{trans}$  values for the boresight  $T_{sys}/\eta$  vs frequency for the X and Y polarizations are shown in Figs. 5a and 5b, respectively. The model results are plotted for 3 representative values for  $L_{trans} = 6.4, 9.1$  & 17.1 cm and  $T_{loss} = 1$  K. The measured values are also shown in these figures for comparison. As seen from Fig. 5a and 5b, the bandwidth performance of the existing system can be increased to  $\geq 300$  MHz by noise matching the PAF to the LNA.

The model aperture efficiency, spillover efficiency and receiver temperature as a function of frequencies are shown in Fig. 5c, 5d and 6a. The aperture efficiency obtained is  $\sim 60\%$  for the three models near 1350 MHz, while the spillover efficiency is  $\sim 98.7\%$ . These values are consistent with the preliminary model results presented in Roshi et al. (2018) [24]. The beamformed receiver temperature is  $\sim 5.5$  K for the new amplifier model and for  $L_{trans} = 9.1$  cm at 1350 MHz. This receiver temperature is about 2 K smaller than the earlier result (see [24]).

The reported aperture efficiency of room temperature PAFs on parabolic reflectors are  $> 70\%$  [43], [44]. The weights for beamforming were obtained by maximizing the SNR for both room temperature PAF observations and our observations. In such maximization, the achieved aperture and spillover efficiencies are function of receiver temperature (see also [30]). Generally the aperture efficiency (non-linearly) increases with increase in receiver temperature. Thus the lower aperture efficiency of  $\sim 60\%$  obtained for our system is a result of lower receiver temperature for the cryogenic PAF. The aperture efficiency of the cryogenic PAF is comparable to a corrugated horn with an edge taper of  $\sim 22$  dB placed at the prime focus of the GBT (S. Srikanth, NRAO, private communication). The spillover efficiency of the PAF, on the other hand, is a factor of  $\sim 1.8$  times better than that achieved with the same corrugated horn.

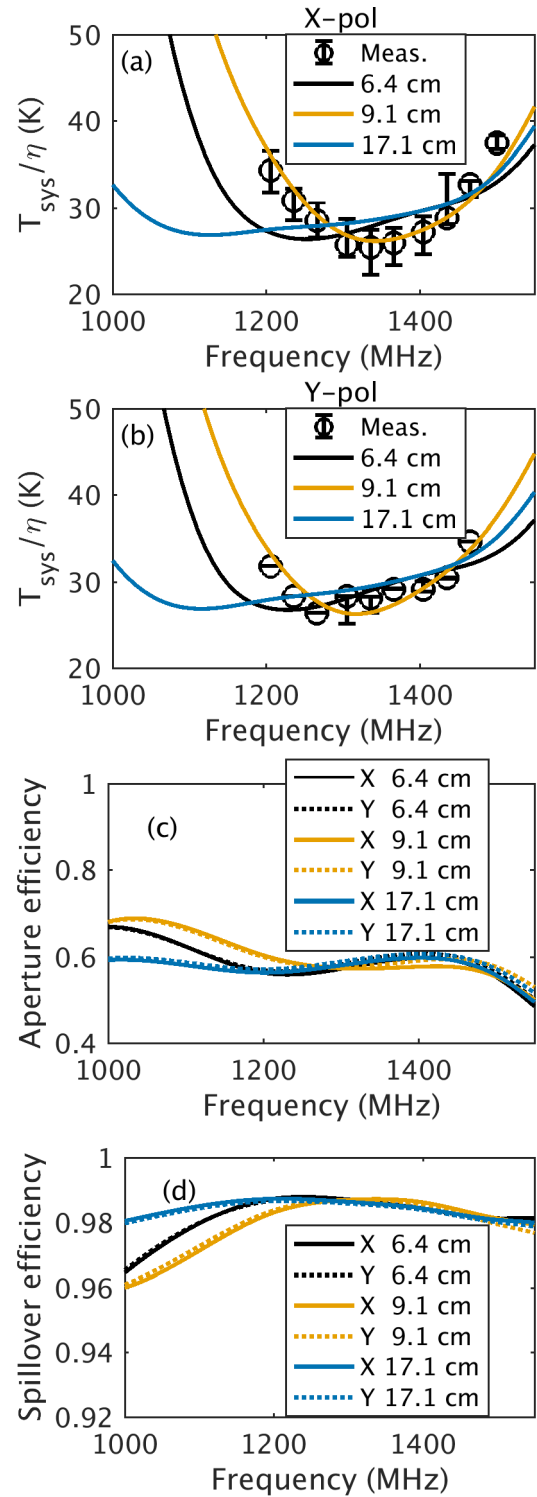


Fig. 5. (a) The modeled boresight  $T_{sys}/\eta$  vs frequency for the X polarization compared with the measured values taken from Roshi et al. (2018) [24]. The measured values are same as those shown in Fig. 4. The PAF model results for the thermal transition lengths  $L_{trans} = 6.4, 9.1$  and 17.1 cm are plotted. All model results are obtained with an additional noise contribution of 1 K to account for the losses ahead of the LNA. (b) Same as (a) but for Y polarization. (c) Model X and Y polarization aperture efficiencies vs frequency for the three thermal transition lengths. (d) Model X and Y polarization spillover efficiencies vs frequency for the three thermal transition lengths.

### B. $\frac{T_{sys}}{\eta}$ over the FoV

The radial distributions (i.e. offset from the boresight) of the measured  $T_{sys}/\eta$  for X and Y polarizations along with

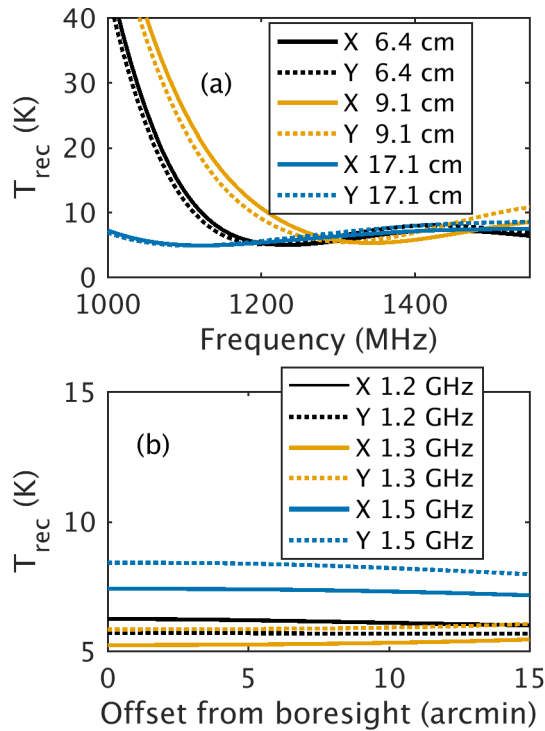


Fig. 6. (a) Model X and Y polarization receiver temperatures vs frequency for three different  $L_{trans}$ . The receiver temperatures are obtained with Eq. 19 using the weights that maximizes the SNR. (b) Model X and Y polarization receiver temperatures vs offset from boresight for frequencies 1.2, 1.3 and 1.5 GHz.

model results are shown in Fig. 7a and 7b respectively. The measurements are made at 1336 MHz. The model results for  $L_{trans} = 9.1$  cm and  $T_{loss} = 1$  K are shown for frequencies 1.2, 1.3 and 1.5 GHz. As seen from Fig. 7a and 7b, the model results for 1.3 GHz compare well with measurements. The model aperture efficiency, spillover efficiency and receiver temperature as a function of offset from boresight are shown in Fig. 7c, 7d and 6b respectively. The performance of the system degrades beyond  $\sim 5'$  because the Airy pattern shifts to the edge of the array and hence there are not enough elements to form a high sensitivity beam (see [24] for further details). Thus the field of view of the PAF is limited by the size of the dipole array.

### C. Receiver temperature

We compare the model receiver temperature with measurements made at the outdoor test facility at the GBO. As mentioned in Section III-C, these measurements are affected by ground scattered radiation. The value of the receiver temperature depends on the weights used to obtain them (see Eq. 19 and also [24]). The receiver temperature that contributes to the system temperature when the PAF is on the telescope can be obtained from the knowledge of the beamformer weights and complex system gain. However, determining the on-telescope receiver temperature is currently not possible since the measurement system has different system gain compared to that on the telescope. Therefore, here we compare model results with the minimum receiver temperature,  $T_{rec,min}$  (see

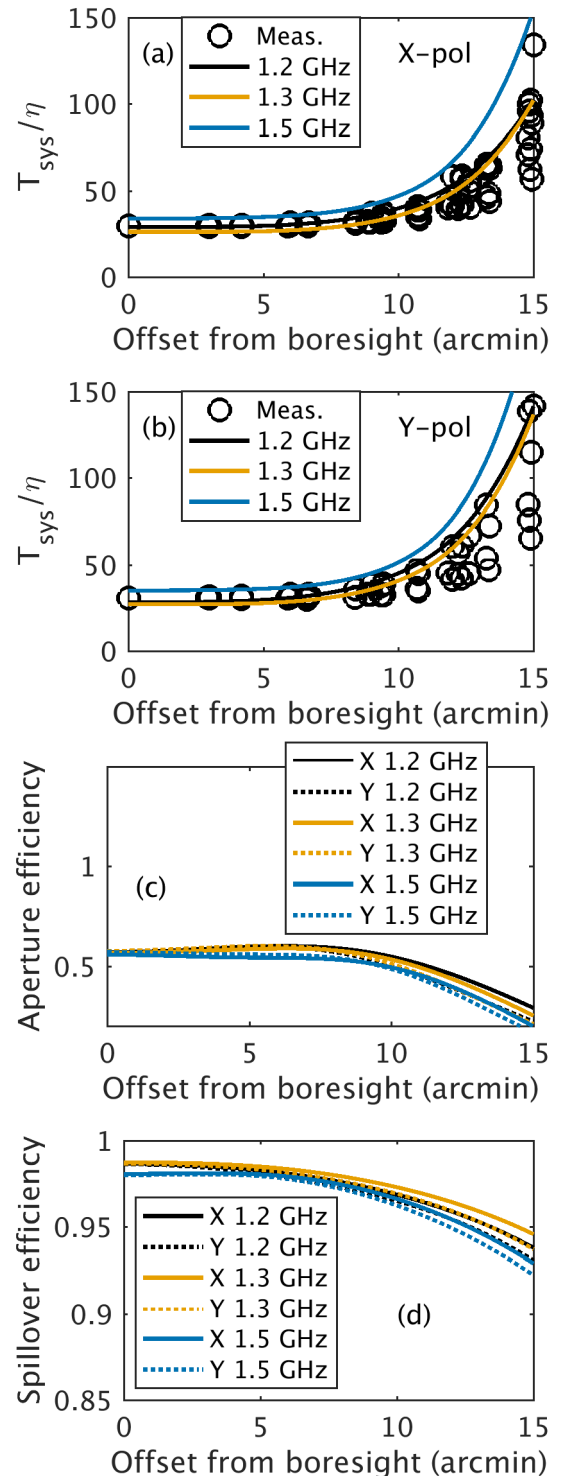


Fig. 7. (a) The measured and modeled  $T_{sys}/\eta$  vs offset from boresight for the X polarization. The measured values at 1336 MHz (taken from [24]) are shown in circles. The PAF model results for  $L_{trans} = 9.1$  cm and  $T_{loss} = 1$  K are plotted for frequencies 1.2, 1.3 and 1.5 GHz. (b) Same as (a) but for Y polarization. (c) Model X and Y polarization aperture efficiencies vs offset from boresight for the three frequencies. (d) Model X and Y polarization spillover efficiencies vs offset from boresight for the three frequencies.

Section III-C). The reference plane and the length of the thermal transition used for these comparisons are, respectively, at the input of the thermal transition (see Fig. 1b) and

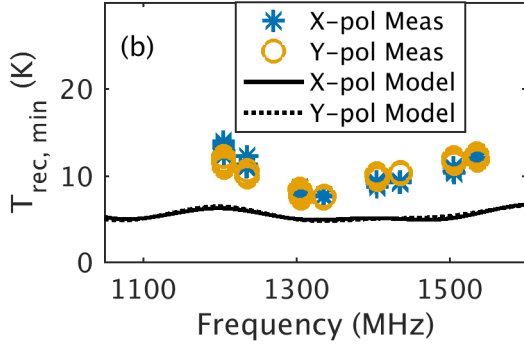


Fig. 8. The minimum receiver temperature  $T_{rec,min}$  obtained from measurement ( see [24]) and the PAF model vs frequency. The model results are for  $L_{trans} = 9.1$  cm and  $T_{loss} = 1$  K. The expected uncertainty in the measured  $T_{rec,min}$  is  $\sim 1.1$  K near 1350 MHz.

$L_{trans} = 9.1$  cm.

We plot  $T_{rec,min}$  obtained from the measurements (see [24]) and that obtained using Eq. 19 vs frequency in Fig. 8. The model values and measurements differ by  $\sim 1.5$  K near 1350 MHz. The difference between model values and measurements increases to  $\sim 5$  K near 1200 and 1500 MHz (see Fig. 8). We believe part of this discrepancy may be due to any uncanceled ground scattering in the measured  $T_{rec,min}$ . Understanding the discrepancy and investigating methods to improve the receiver temperature measurements are ongoing research activity.

#### D. Uncertainty in the model results

The model uses a set of input parameters and results obtained from electromagnetic simulation of the dipole array. Currently, the uncertainties in both these quantities are not well determined. Further, the accuracy of the measured results against which model predictions are compared are currently limited by systematic errors.

We expect that the accuracy of the model results is dominated by the uncertainty in the input parameters to the computational model. The embedded beam patterns and impedance matrix are obtained from the output of the CST MWS simulation with solver mesh size  $\lambda/20$ . We found that our CST simulation results have comparable values with results obtained from HFSS<sup>5</sup> (Warnick, private communication) as well as those obtained from the CST with a coarser mesh ( $\lambda/10$ ) size. However, a direct comparison of the field patterns and S-parameters with measurements is currently not available. The secondary fields due to reflections from the telescope surface are computed using a geometric optics approximation, but we have not quantified the inaccuracies in this computation. The uncertainties in the other input parameters are discussed in Section II, III-C & III-D. To obtain an uncertainty for the model results, we estimate the results by changing the input parameters by an amount equal to their uncertainties. The estimated variation in the model values for  $T_{sys}/\eta$  for  $L_{trans} = 9.1$  cm and  $T_{loss} = 1$  K is  $\sim 15\%$  near 1350 MHz. This uncertainty in the model result is valid over a frequency range of  $\sim 150$  MHz centered at 1350 MHz.

<sup>5</sup><http://www.ansys.com/products/electronics/ansys-hfss>

## V. CONCLUSION

In this paper, we have presented a model for noise matched phased array feed system. The PAF model predictions were then compared with measurement results. The measurements were made with a cryogenic 19 element dual polarized PAF mounted on the GBT. This PAF was designed to operate over a frequency range  $\geq 150$  MHz centered at 1350 MHz. Our main results were:

- 1) We have derived a new expression for the covariance matrices for signal by applying the Lorentz reciprocity theorem. An expression for the receiver noise covariances matrix and noise temperature were derived in terms of the Lange invariants, which were advantageous for noise matching the PAF for optimum performance.
- 2) We have shown that the PAF model predictions compare well with the measured  $T_{sys}/\eta$  made on the GBT, both as a function of frequency and as a function of offset from boresight.
- 3) Our modeling have indicated that the bandwidth performance of the PAF could be improved by a factor of two (i.e.  $\geq 300$  MHz) compared to the current performance by noise matching the PAF to the LNA.
- 4) The PAF model results differ by  $\sim 5$  K (maximum) from the measured minimum receiver temperature. Investigation to understand this discrepancy and to improve receiver temperature measurements are underway.

## APPENDIX A

The power spectral density due to receiver noise can be converted to a physical temperature using the definition of noise figure [35] (see also [21]). *In the absence of a matching network*, the receiver temperature of the PAF can be obtained using Eq. 17 as [32]

$$T_{rec} = T_0 \frac{\mathbf{w}_1^H \left( R_n \mathcal{I} + \sqrt{R_n g_n} (\rho \mathbf{Z} + \rho^* \mathbf{Z}^H) + g_n \mathbf{Z} \mathbf{Z}^H \right) \mathbf{w}_1}{\frac{1}{2} \mathbf{w}_1^H (\mathbf{Z} + \mathbf{Z}^H) \mathbf{w}_1}. \quad (21)$$

Equation 21 can be rewritten as

$$\begin{aligned} & \frac{1}{2} \mathbf{w}_1^H (\mathbf{Z} + \mathbf{Z}^H) \mathbf{w}_1 \frac{T_{rec}}{T_0} \\ &= \mathbf{w}_1^H \left( R_n \mathcal{I} + \sqrt{R_n g_n} (\rho \mathbf{Z} + \rho^* \mathbf{Z}^H) + g_n \mathbf{Z} \mathbf{Z}^H \right) \mathbf{w}_1 \\ &= \mathbf{w}_1^H \left( 2 \sqrt{R_n g_n} (1 - \rho_i^2) \text{Re}\{\mathbf{Z}\} + \right. \\ & \quad \left. 2 \rho_r \sqrt{R_n g_n} \text{Re}\{\mathbf{Z}\} \right) \mathbf{w}_1 + \\ & \quad \mathbf{w}_1^H \left( \frac{R_n g_n}{g_n} \mathcal{I} + g_n \mathbf{Z} \mathbf{Z}^H - 2 \sqrt{R_n g_n} (1 - \rho_i^2) \text{Re}\{\mathbf{Z}\} \right. \\ & \quad \left. - 2 \rho_i \sqrt{R_n g_n} \text{Im}\{\mathbf{Z}\} \right) \mathbf{w}_1 \\ &= 2 \left( \sqrt{R_n g_n} (1 - \rho_i^2) + \rho_r \sqrt{R_n g_n} \right) \frac{1}{2} \mathbf{w}_1^H (\mathbf{Z} + \mathbf{Z}^H) \mathbf{w}_1 + \\ & \quad \mathbf{w}_1^H \left( \frac{R_n g_n}{g_n} \mathcal{I} + g_n \mathbf{Z} \mathbf{Z}^H - 2 \sqrt{R_n g_n} (1 - \rho_i^2) \text{Re}\{\mathbf{Z}\} \right. \\ & \quad \left. - 2 \rho_i \sqrt{R_n g_n} \text{Im}\{\mathbf{Z}\} \right) \mathbf{w}_1 \end{aligned}$$

$$\begin{aligned}
 &= \frac{T_{min}}{T_0} \frac{1}{2} \mathbf{w}_1^H (\mathbf{Z} + \mathbf{Z}^H) \mathbf{w}_1 + \\
 &\quad \mathbf{w}_1^H \left( g_n |Z_{LNAopt}|^2 \mathcal{I} + g_n \mathbf{Z} \mathbf{Z}^H - \right. \\
 &\quad \quad \left. 2 g_n \operatorname{Re}\{Z_{LNAopt}\} \operatorname{Re}\{\mathbf{Z}\} - \right. \\
 &\quad \quad \left. 2 g_n \operatorname{Im}\{Z_{LNAopt}\} \operatorname{Im}\{\mathbf{Z}\} \right) \mathbf{w}_1 \\
 &= \frac{T_{min}}{T_0} \frac{1}{2} \mathbf{w}_1^H (\mathbf{Z} + \mathbf{Z}^H) \mathbf{w}_1 + \\
 &\quad g_n \mathbf{w}_1^H (\mathbf{Z} - Z_{LNAopt} \mathcal{I}) (\mathbf{Z} - Z_{LNAopt} \mathcal{I})^H \mathbf{w}_1 \\
 &= \frac{T_{min}}{T_0} \frac{1}{2} \mathbf{w}_1^H (\mathbf{Z} + \mathbf{Z}^H) \mathbf{w}_1 + \\
 &\quad N \frac{\mathbf{w}_1^H (\mathbf{Z} - Z_{LNAopt} \mathcal{I}) (\mathbf{Z} - Z_{LNAopt} \mathcal{I})^H \mathbf{w}_1}{\operatorname{Re}\{Z_{LNAopt}\}} \quad (22)
 \end{aligned}$$

Eq. 22 can be readily rewritten as Eq. 19.

## APPENDIX B

$A_{ap}$	Aperture area of the telescope
$\mathbf{G}$	Diagonal matrix of overall system gain
$g_n, R_n, \rho$	Noise parameters of the LNA
$\mathcal{I}$	Identity matrix
$\mathbf{I}_0$	Vector of port currents
$k_B$	Boltzmann constant
$L_{trans}$	Length of the thermal transition
$\mathbf{M}$	Characteristic matrix of the PAF system
$N$	Lange invariant
$\mathbf{R}_{loss}$	Open circuit voltage covariance (OCVC) matrix due to the losses ahead of the LNA
$\mathbf{R}_{rec}$	OCVC matrix due to the receiver noise
$\mathbf{R}_{signal}$	OCVC matrix due to the source
$\mathbf{R}_{sky}$	OCVC matrix due to the sky background and atmospheric noise
$\mathbf{R}_{spill}$	OCVC matrix due to the spillover noise
$S_{source}$	Flux density of the source
$T_0$	Reference temperature, 290 K
$T_g$	Ground temperature (300 K)
$T_{loss}$	Temperature due to losses ahead of the LNA
$T_{min}$	Minimum LNA noise temperature
$T_{rec,min}$	Minimum receiver temperature
$T_{spill}$	Spillover temperature
$T_{sys}$	System temperature
$\tilde{\mathbf{V}}$	Voltage vector at the beamformer input
$\mathbf{V}_{oc}$	Open circuit voltage vector
$\mathbf{w}$	Weight vector applied at the beamformer
$\mathbf{w}_1$	Modified weight vector when using OCVC matrix
$\mathbf{Z}$	Impedance matrix of the PAF
$Z_0$	Free space impedance
$z_0$	Reference impedance, 50 $\Omega$
$Z_{in}$	Input impedance of the receiver system at the reference plane
$\mathbf{Z}_{in}$	Diagonal matrix of elements $Z_{in}$
$Z_{LNA}$	Input impedance of the LNA
$Z_{LNAopt}$	Optimum impedance of the LNA
$Z_{opt}$	Value of $Z_{LNAopt}$ at the reference plane
$\eta_{ap}$	Aperture efficiency
$\eta_{spill}$	Spillover efficiency
$\eta$	Product of $\eta_{ap}$ and PAF's radiation efficiency
$\vec{\psi}^e, \vec{\Psi}^e$	Vectors of embedded beam patterns
$\vec{\psi}_{pap}^e$	Vectors of embedded beam patterns propagated to the projected aperture plane

## ACKNOWLEDGMENT

The authors would like to acknowledge very useful discussions and suggestions from Matt Morgan during the initial phase of the development of the PAF model. The possibility of an analytical solution for PAF problem was pointed out to D. A. Roshi by Stuart Hay, CSIRO. The authors acknowledge the efforts of Bob Simon, Steve White and other Green Bank Observatory and NRAO Technology Center staff in successfully building and testing the PAF receiver. We thank Marian Pospieszalski, Anthony Kerr for useful discussions on the noise properties of the receiver, Srikanth for discussions on

the computation of the GBT aperture field, Wavley Groves and Matt Morgan for providing the amplifier noise model, Robert Dickman and S. K. Pan for the support and useful discussions during the course of this work. We thank the referees for providing very useful comments and suggestions, which has significantly improved the paper.

## REFERENCES

- [1] J. R. Fisher and R. F. Bradley, "Full-sampling array feeds for radio telescopes," in *Proceedings of SPIE*, Munich, Germany, Jul. 2000, pp. 308–318.
- [2] T. Oosterloo, M. Verheijen, and W. van Cappellen, "The latest on Apertif," in *Proceedings of the ISKAF2010 Science Meeting*, Assen, the Netherlands, Jun. 2010, pp. 43–54.
- [3] B. Veidt *et al.*, "Demonstration of a dual-polarized phased-array feed," *IEEE Transactions on Antennas and Propagation*, vol. 59, no. 6, pp. 2047–2057, June 2011.
- [4] G. Cortes-Medellin *et al.*, "A fully cryogenic phased array camera for radio astronomy," *IEEE Trans. Antennas and Propagation*, vol. 63, pp. 2471–2481, Jun. 2015.
- [5] A. P. Chippendale, A. J. Brown, R. J. Beresford, G. A. Hampson, A. Macleod, R. D. Shaw, M. L. Brothers, C. Cantrall, A. R. Forsyth, S. G. Hay, and M. Leach, "Measured sensitivity of the first Mark II phased array feed on an ASKAP antenna," in *2015 International Conference on Electromagnetics in Advanced Applications (ICEAA)*. IEEE, 2015, pp. 541–544.
- [6] Y. Wu, C. Jin, J. Fan, X. Zhao, L. Yu, and B. Du, "Development of the L-band phased array feed for the Five-hundred-meter Aperture Spherical radio Telescope," in *Progress in Electromagnetic Research Symposium (PIERS)*, Shanghai, China, Aug. 2016, pp. 1667 – 1667.
- [7] S. G. Hay and T. S. Bird, *Applications of Phased Array Feeders in Reflector Antennas*, 1st ed., Z. N. Chen, Ed. Singapore: Springer, 2015.
- [8] K. F. Warnick, R. Maaskant, M. V. Ivashina, D. B. Davidson, and B. D. Jeffs, "High-sensitivity phased array receivers for radio astronomy," *Proceedings of the IEEE*, vol. 104, pp. 607–622, Mar. 2016.
- [9] C. Craeye and D. González-Ovejero, "A review on array mutual coupling analysis," *Radio Science*, vol. 46, p. 25, Apr. 2011.
- [10] J. R. Fisher, "Phased array feed for low noise reflector antenna," National Radio Astronomy Observatory, NRAO Electronic Division Internal Report 307, 1996.
- [11] K. F. Warnick and M. A. Jensen, "Effects of mutual coupling on interference mitigation with a focal plane array," *IEEE Transactions on Antennas and Propagation*, vol. 53, no. 8, pp. 2490–2498, August 2005.
- [12] R. Maaskant and E. E. M. Woestenburger, "Applying the active antenna impedance to achieve noise match in receiving array antennas," in *Antennas and Propagation Society International Symposium, 2007 IEEE*, Honolulu, HI, USA, Jun. 2007, pp. 5889 – 5892.
- [13] K. F. Warnick and M. A. Jensen, "Optimal noise matching for mutually-coupled arrays," *IEEE Transactions on Antennas and Propagation*, vol. 55, no. 6, pp. 1726–1731, June 2007.
- [14] S. G. Hay and J. D. O'Sullivan, "Analysis of common-mode effects in a dual-polarized planar connected-array antenna," *Radio Science*, vol. 43, pp. 1–9, Dec. 2008.
- [15] K. F. Warnick, B. Woestenburger, L. Belostotski, and P. Russer, "Minimizing the noise penalty due to mutual coupling for a receiving array," *IEEE Trans. Antennas Propag.*, vol. 57, pp. 1634–1644, Jun. 2009.
- [16] R. Maaskant, "Analysis of large antenna systems," Ph.D. dissertation, Technische Universiteit Eindhoven, Eindhoven, Jun. 2010. [Online]. Available: <http://alexandria.tue.nl/extra2/201010409.pdf>
- [17] K. F. Warnick *et al.*, "Design and Characterization of an Active Impedance Matched Low-Noise Phased Array Feed," *IEEE Trans. Antennas Propag.*, vol. 59, pp. 1876–1885, Jun. 2011.
- [18] S. G. Hay, "Maximum-Sensitivity Matching of Connected-Array Antennas Subject to Lange Noise Constants," *Int. Journal of Microw. and Optical Tech.*, vol. 5, pp. 375–383, Nov. 2010.
- [19] K. F. Warnick and B. D. Jeffs, "Efficiencies and system temperature for a beamforming array," *IEEE Antennas and Wireless Propagation Letters*, vol. 7, pp. 565–568, 2008.
- [20] —, "Gain and aperture efficiency for a reflector antenna with an array feed," *IEEE Antennas and Wireless Propagation Letters*, vol. 5, pp. 499–502, 2006.
- [21] K. Warnick, M. Ivashina, R. Maaskant, and B. Woestenburger, "Unified Definitions of Efficiencies and System Noise Temperature for Receiving Antenna Arrays," *IEEE Transactions on Antennas and Propagation*, vol. 58, no. 6, pp. 2121–2125, Jun. 2010.
- [22] M. V. Ivashina, R. Maaskant, and B. Woestenburger, "Equivalent system representation to model the beam sensitivity of receiving antenna arrays," *IEEE Antennas and Wireless Propagation Letters*, vol. 7, pp. 733–737, Oct. 2008.
- [23] L. Belostotski, B. Veidt, K. Warnick, and A. Madanayake, "Low-noise amplifier design considerations for use in antenna arrays," *IEEE Trans. Antennas and Propagation*, vol. 63, pp. 2508–2520, Jun. 2015.
- [24] D. A. Roshi *et al.*, "Performance of a highly sensitive, 19-element, dual-polarization, cryogenic Phased Array Feed," *Astronomical Journal*, vol. 155, no. 5, p. 18, May 2018.
- [25] R. Hall and L. J. King, "The Green Bank Telescope," in *Antennas and Propagation Society International Symposium, 1992.*, Chicago, USA, Jun. 1992, pp. 862–865.
- [26] R. Norrid and S. Srikanth, "A summary of the GBT optics," National Radio Astronomy Observatory (NRAO), GBT memo 155, 1996.
- [27] W. M. Groves-III and M. A. Morgan, "A Cryogenic SiGe Low-noise Amplifier Optimized for Phased-array Feeds," *Publications of the Astronomical Society of Pacific*, vol. 129, p. 085001, Jul. 2017.
- [28] M. W. Pospieszalski, "Interpreting transistor noise," *IEEE Microw. Mag.*, vol. 11, pp. 61–79, Oct. 2010.
- [29] J. Lange, "Noise characterization of linear twoports in terms of invariant parameters," *IEEE J. Solid-State Circuits*, vol. 2, pp. 37–40, Jun. 1967.
- [30] B. D. Jeffs, K. F. Warnick, J. Landon *et al.*, "Signal Processing for Phased Array Feeds in Radio Astronomical Telescopes," *IEEE Journal of Selected Topics in Signal Processing*, vol. 2, pp. 635–646, Oct. 2008.
- [31] R. C. Hansen, *The Handbook of Antenna Design*, 1st ed., A. W. Rudge *et al.*, Eds. London, UK: Peter Peregrinus Ltd., 1983.
- [32] D. A. Roshi and J. R. Fisher, "A Model for Phased Array Feed," National Radio Astronomy Observatory, NRAO Electronic Division Internal Report 330, 2016. [Online]. Available: [http://library.nrao.edu/public/memos/edir/EDIR\\_330.pdf](http://library.nrao.edu/public/memos/edir/EDIR_330.pdf)
- [33] D. A. Roshi, "Phased Array Feed Model Equations corresponding to two definitions of embedded beam pattern," National Radio Astronomy Observatory, NRAO Electronic Division Internal Report 331, 2017. [Online]. Available: [http://library.nrao.edu/public/memos/edir/EDIR\\_331.pdf](http://library.nrao.edu/public/memos/edir/EDIR_331.pdf)
- [34] R. H. Clarke and J. Brown, *Diffraction Theory and Antennas*. West Sussex, England: Ellis Horwood Limited, 1980.
- [35] A. R. Kerr and J. Randa, "Thermal noise and noise measurements – a 2010 update," *IEEE Microw. Mag.*, vol. 11, pp. 40–52, Oct. 2010.
- [36] R. Q. Twiss, "Nyquist's and Thevenin's theorems generalized for non-reciprocal linear networks," *J. Appl. Phys.*, vol. 26, no. 5, pp. 599–602, May 1955.
- [37] J.-Y. Delahaye, P. Gole, and P. Waldteufel, "Calibration error of L-band sky-looking ground-based radiometers," *Radio Science*, vol. 37, p. 11, Feb. 2002.
- [38] P. Reich and W. Reich, "A radio continuum survey of the northern sky at 1420 MHz. II," *A&AS*, vol. 63, pp. 205–292, Feb. 1986.
- [39] A. D. Yaghjian, "Equivalence of surface current and aperture field integrations for reflector antennas," *IEEE Trans. Antennas and Propagation*, vol. 32, pp. 1355–1357, Dec. 1984.
- [40] E. E. M. Woestenburger, L. Bakker, and M. V. Ivashina, "Experimental Results for the Sensitivity of a Low Noise Aperture Array Tile for the SKA," *IEEE Transactions on Antennas and Propagation*, vol. 60, no. 2, pp. 915–921, February 2012.
- [41] A. P. Chippendale, D. B. Hayman, and S. G. Hay, "Measuring Noise Temperatures of Phased-Array Antennas for Astronomy at CSIRO," *Publications of the Astronomical Society of the Pacific*, vol. 31, pp. 1–14, Feb. 2014.
- [42] R. A. Perley and B. J. Butler, "An Accurate Flux Density Scale from 50 MHz to 50 GHz," *The Astrophysical Journal Supplement Series*, vol. 230, p. 18, May 2017.
- [43] W. van Cappellen and L. Bakker, "APERTIF: Phased array feeds for the Westerbork Synthesis Radio Telescope," in *Phased Array Systems and Technology (ARRAY), 2010 IEEE International Symposium on*. IEEE, 2010, pp. 640–647.
- [44] A. P. Chippendale, R. J. Beresford, X. Deng, M. Leach, J. E. Reynolds, M. Kramer, and T. Tzioumis, "Testing a modified ASKAP Mark II phased array feed on the 64 m Parkes radio telescope," in *2016 International Conference on Electromagnetics in Advanced Applications (ICEAA)*. IEEE, 2016, pp. 909–912.

PLACE  
PHOTO  
HERE

**D. Anish Roshi** graduated with an engineering degree in electronics and communications from the University of Kerala in 1988. He then joined the Tata Institute of Fundamental Research (TIFR), National Center for Radio Astrophysics, Pune as a Research Associate/Scientific Officer. At TIFR, he completed his Ph.D (Physics) specializing in Radio Astronomy (1999) and was appointed as a member of the faculty. He was a Jansky postdoctoral fellow at the National Radio Astronomy Observatory (NRAO), USA between 2000 and 2002. On completion of the

post doctoral fellowship, Dr Roshi joined the Raman Research Institute (RRI), Bangalore. While at RRI, he was involved with several Astrophysics research and instrumentation projects. He led a team of engineers to build a digital receiver for the Murchison Widefield Array, located at Western Australia. In 2010, Dr. Roshi moved to the National Radio Astronomy Observatory (NRAO), USA as a member of the scientific staff. At NRAO, he was the System Architect and Project Scientist for the Versatile Astronomical Spectrometer that was built for the Green Bank Telescope (GBT). He was also the System Architect of the Phased Array Feed/Beamformer project. He is currently a Senior Observatory Scientist for Radio Astronomy at the Arecibo Observatory. His research interests include Galactic interstellar medium, massive star formation and radio astronomy instrumentation.

PLACE  
PHOTO  
HERE

**William Shillue** is a Research Engineer at the National Radio Astronomy Observatory (NRAO), Central Development Laboratory (CDL), Charlottesville, VA. He received the BS degree in electrical engineering from Cornell University in 1985, and an MS degree in electrical engineering from Univ. of Massachusetts in 1990. In 1991 he joined the National Radio Astronomy Observatory (NRAO) in Green Bank, WV, and participated in the design and deployment of a 13.7-m satellite earth station in support of the NASA Orbiting-Very-Long-Baseline-

Interferometer Project. From 1994-2005 he worked at NRAO Tucson developing millimeter-wave receivers and instrumentation for the 12-m telescope, and new photonics technologies for the Atacama Large Millimeter Array (ALMA). From 2005-2012, he was team leader for the ALMA Central Local Oscillator and ALMA photonic LO distribution systems. More recently, he has led the NRAO Phased Array Research and Development program and developed technology concepts for next generation radio astronomy instrumentation. He is a member of IEEE Photonics Society and Microwave Theory and Techniques Society.

PLACE  
PHOTO  
HERE

**J. Richard Fisher** was born in Pittsburgh, PA in 1943 but he spent his school years on a small farm near Reynoldsville in western Pennsylvania. He received a BS in physics from Penn State in 1965 and a PhD in astronomy from the University of Maryland in 1972. He joined the NRAO scientific staff at Green Bank, WV immediately following graduate school and has held various positions such as Head of the Electronics Division, Site Director, and Project Manager of several instrumentation projects. In 1978 he took leave from the NRAO to

spend 18 months at the Division of Radio Physics, CSIRO in Australia and 3 months at the Raman Research Institute in Bangalore, India. He moved to the Charlottesville, VA offices of NRAO in 2005 and held the position of Chief Technologist until his retirement in 2012. He is now Scientist Emeritus at NRAO. His research interests include cosmology, antenna design, and signal processing.